Construction and Building Materials 305 (2021) 124794

Contents lists available at ScienceDirect

Construction and Building Materials

journal homepage: www.elsevier.com/locate/conbuildmat

Effect of carbonation on bulk resistivity of cement/carbon nanofiber composites

Kamila Gawel *, Sigurd Wenner, Laura Edvardsen

SINTEF Industry, Trondheim, Norway

ARTICLE INFO

Keywords:
Cement
Composite
Carbon nanofibers
Conductive
Bulk resistivity
Carbonation

ABSTRACT

The conductivity of cement/carbon nanofiber (CNF) composite materials has previously been shown to be affected by parameters such as e.g. CNF content or water to cement (w/c) ratios, water saturation and temperature. However, whether and to what extent chemical processes like cement carbonation can affect the electrical conductivity of cement/CNF materials remains unexplored. To investigate this the resistivity changes upon carbonation of Portland G cement/CNF composites were followed for more than 4 months. An increase in resistivity was observed within the first weeks of carbonation followed by a plateau and a subsequent decrease after 4 months. The changes in resistivity were correlated with the progress of the carbonation front followed using X-ray tomography. The magnitude of the resistivity changes was found to be related to w/c ratio. Volumetric changes affecting the connectivity between the CNFs can explain the resistivity changes.

1. Introduction

Cement materials containing carbon nanofibers (CNF) can be conductive and piezoresistive [1-8]. Piezoresistivity relies on the changes of electrical resistivity upon exposure to mechanical load. The load sensitivity and conductivity makes the hybrid cement materials suitable as sensors in e.g. structural health monitoring of reinforced concrete structures [2,9] and traffic monitoring [10-12]. The hybrid cement materials function as signal transducers that translate changes in mechanical load or mechanical failure into changes in electrical properties like e.g. conductivity. The structural health monitoring of conductive concrete relies on an increase in effective resistivity when fractures start to propagate in the structure [13,14]. In a traffic monitoring system, piezoresistive properties of hybrid cement materials are utilized. The number of cars passing through a chosen road section is counted based on the number of peaks in the conductivity, caused by load imparted by the passing car.

The mechanism explaining the piezoresistivity phenomenon is related to the connectivity within the network of conductive particles in a nonconductive matrix. When mechanical load is applied to a material containing electrically conductive particles, the inter-particle distance decreases, and new conductive paths are created. An increased number of inter-particle connections leads to a higher material conductivity [15]. The percolation threshold defines the onset of conductive path formation, when particle network transforms from being separated to connected [16-18]. This threshold is related to particle type, shape, aspect ratio and the quality of dispersion in the nonconductive matrix.

In addition to nanoparticle-related parameters, the resistivity of cements containing carbon nanofibers is strongly related to other compositional parameters like water to cement ratio (w/c) and water content in the pore structure [18-20]. Water was shown to act as an insulator that decreases the conductivity of the material, so that water removal upon drying of cement-CNF samples leads to a conductivity increase [19,20]. The conductive properties have also been shown to be sensitive to water to cement ratio i.e. to the amount of water that is consumed during the cement hydration processes [20]. It has been suggested that the material resistivity may be dependent on the amount of hydration products precipitated during cement hydration processes [20]. Given that the conductive properties of cement/CNF materials are very sensitive to water content and the amount of material precipitated within the structure, it has been hypothesized that these materials may also be sensitive to cement carbonation.

Cement carbonation is a reaction of cement with CO_2 in the presence of water [21-25]. It involves the following chemical processes [25]: (1) dissolution of cement hydration products, (2) carbonation of cement hydration products and formation of calcium carbonate, (3) dissolution of calcium carbonate and leaching of calcium from the cement to the solution. While the second stage of the carbonation processes leads to

* Corresponding author.
E-mail address: kamila.gawel@sintef.no (K. Gawel).

https://doi.org/10.1016/j.conbuildmat.2021.124794
Received 21 April 2021; Received in revised form 27 August 2021; Accepted 1 September 2021
Available online 11 September 2021

decrease in material porosity and increase in density which may have a positive impact on the hydraulic and mechanical properties of the material, the third stage leads to etching of the cementitious material and is deteriorative for the mechanical and hydraulic properties of the cement. Therefore, the carbonation is most often considered as a degradation process and is strongly undesired. The current state of the art literature is missing a comprehensive description of carbonation processes in hybrid cement/CNF materials. The carbonation processes are related with structural and volumetric changes inside the cement matrix [26,27]. Whether or not such changes affect resistivity of cement/CNF is a knowledge gap that this paper aims to fill.

The sensitivity of cement/CNF materials to carbonation is important in view of using these materials in monitoring applications. It is important to define to what extent the signal can be affected by chemical degradation processes like carbonation, which is by far the most common degradation occurring at atmospheric conditions.

To this end the resistivity of cement/CNF hybrid materials was followed during carbonation. This paper presents observed changes in resistivity, and correlates them with propagation of the carbonation front monitored by X-ray tomography. The carbonation rates of cement/CNF and reference (without CNF) samples were compared. Potential mechanisms responsible for the observed changes are discussed.

Knowledge gained in this study gives new insight into structural health monitoring of cement construction elements and may open for other, new monitoring applications in e.g. carbon dioxide storage, environmental monitoring etc.

2. Materials and methods

2.1. Preparation of cement-CNF materials

Pyrograf PR-19 XT-LHT nanofibers (CNF) supplied by Applied Sciences Inc. were used to prepare the cement/CNF samples. The CNFs were heated at temperatures of 1500 °C by the supplier. This heat treatment was performed to carbonize vapor-deposited carbon present on CNF surfaces. According to the supplier, such a heat treatment provides the highest electrical conductivity in nanocomposites. The average diameter of PR-19 fibers is about 150 nm and the average length is in the range of 50–200 μm.

CNFs are hydrophobic particles and as such they require application of dispersing agents to improve the homogeneity of CNFs in cement slurry. CNF fibers were dispersed in water/dispersing agent solution, where MasterGlenium SKY 899 (BASF) superplasticizer polymer (SP) was used as the dispersing agent. The CNF dispersion was prepared by mixing 300 g of water with 20 g of CNFs and 8 g of SP. CNF to dispersant weight ratio used in this work was 5:2. Based on preliminary tests, this ratio was found to give a favourable dispersion of CNFs. CNF dispersion (12.5 g) was hand mixed with Portland G cement (from Norcem) (25 g) and additional water to yield the water to cement ratios given in Table 1 (1, 3 and 5 g for samples D1, D2 and D3 respectively)

Samples with w/c ratio ranging between 0.49 and 0.66 were prepared. The CNF/cement weight ratio was constant and kept at 0.03 for all samples. The cement/CNF slurry was hand-mixed for three minutes before it was placed in plastic cylinder molds. Samples in two sizes were obtained. The large samples (A1 and REF) had a diameter of 12 mm while small samples (D1, D2, D3 and P1) had a diameter of 5.5 mm. After one day of hardening at ambient conditions, the samples were placed in sealed plastic bags to prevent water evaporation. After four months of further hardening the metal connectors were glued to the cylinder ends using a conductive (silver nanoparticles filled) epoxy resin (EpoTek, H21D). The epoxy resin was left to harden for the next three days. Fig. 1 presents photographs of samples D1, D2, D3 and P1 with attached electrical connectors (Cu wires (samples D) and Cu plates (sample P1).

2.2. Exposure to CO_2-saturated water

The prepared samples were first equilibrated in deionized water overnight before they were exposed to CO_2-saturated deionized water. Unicyl CO_2 supplied by AGA/Linde was used to saturate water at atmospheric conditions (T ~ 23 °C, atmospheric pressure). At atmospheric pressure pH of CO_2-saturated deionized water is around 5.5. The pH of the solution was kept around this value by constant injection of CO_2 into the solution. **X-ray micro-computed tomography (μ-CT)**

X-ray micro-computed tomography (μ-CT) was used to follow the dynamics of carbonation of reference and cement/CNF samples. Scanning was performed after the samples had been exposed to the CO_2-saturated water for 7, 14, 21, 49, 101 and 136 days. After the given time the samples were removed from the CO_2 saturated solution for 2 h (time needed for transport and CT scanning of samples). An industrial CT scanner (XT H 225 ST) was used. It was operated at 210 kV and with a current of 155 μA. The raw CT data were reconstructed into cross sectional slices.

The tomography cross-sectional images were analyzed using the "Radial Profile" plugin in the ImageJ software. This plugin produced a profile plot of normalized integrated intensities around concentric circles as a function of distance from the center of the cylindrical samples.

2.3. Resistance measurements

Changes in sample resistance, as a result of sample exposure to CO_2-saturated water, were followed using a Fluke 117 True RMS multimeter. Resistance (R) between connectors was measured for all samples after different exposure times to CO_2-saturated water solution. The bulk resistivity (ρ, also called volume resistivity) of materials can be calculated according to Eq. (1)

$$\rho = R^{*}A/l \quad (1)$$

where: R is the electrical resistance measured between connectors; A is the surface area of the connector; l is the distance between connectors.

As the sizes of samples D1, D2, D3 and P1 were identical, the bulk resistivity values are proportional to resistance with the same

Table 1
Sample overview indicating weight ratios between CNF, water, dispersant and cement as well as the connection type used for each sample and the purpose in this paper.

Sample name	CNF/cement	Water/cement	Dispersant/cement	Connection type	Diameter [mm]	Length [mm]	Purpose**
REF	0	0.58	0.012	–	12	18	Carbonation dynamics
A1	0.03	0.58	0.012	–	12	18	
D1	0.03	0.49	0.012	Cu wire	5.5	18	Resistance measurements
D2	0.03	0.58	0.012	Cu wire	5.5	18	
D3	0.03	0.66	0.012	Cu wire	5.5	18	
P1*	0.03	0.49	0.012	Cu plate	5.5	18	

*Please note: Sample P1 has identical composition as sample D1 and only material used for electrical connection is different. The P1 sample was used to test the reproducibility of the results.

**Large samples were used to follow carbonation dynamics in situ with X-ray tomography. To achieve carbonation in a larger volume fraction and enable observation of significant changes in resistivity, samples with smaller diameter were used.

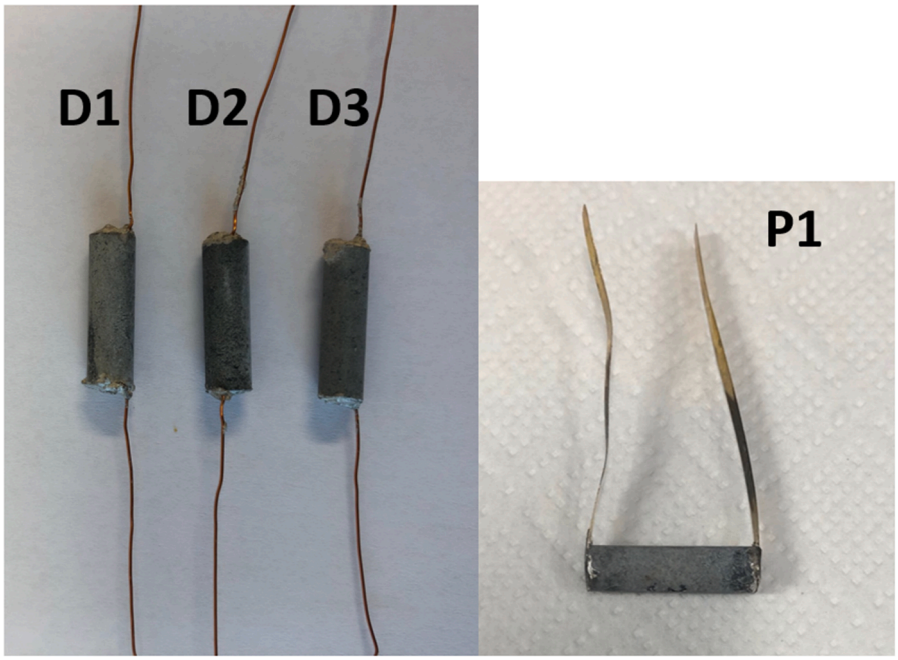

Fig. 1. Photographs of samples D1, D2, D3 and P1 with attached electrical connectors (Cu wires (samples D) and Cu plates (sample P1)). P1 sample was used to test reproducibility.

proportionality coefficient ($A/l = 8.83 \times 10^{-4}$ m) for all samples.

2.4. Scanning electron microscopy (SEM)

To image the cross-section of the A1 and REF samples after 59 days of exposure to CO_2-saturated water, the samples were dried in an oven at 40 °C for one week, then cut in half and finally polished using fine grade grinding paper.

Energy-dispersive X-ray spectroscopy (EDS) maps of the cross-sections were acquired using a Hitachi S3400N microscope equipped with an Oxford X-MAX 80 detector. The acceleration voltage was 15 kV, the working distance was 10 mm. To neutralize electrostatic charging, an air pressure of 10 Pa was retained in the microscope chamber. Quantitative maps of C and O were created using the Oxford Aztec software.

2.5. Focused ion beam (FIB)-SEM tomography

The focused ion beam (FIB)-SEM tomography was used to verify whether the carbon nanofibers dispersed in carbonated cement matrix form a continuous (percolating) network. It was performed as follows. Small pieces (50–100 μm) were chipped off the (carbonated) sides of the cylindrical A1 cement sample, suspended in isopropanol and dispersed on an aluminum stub. The stub was then coated with 50 nm Au using a sputter coater to prevent electrostatic charging. A FEI Helios G4 instrument was used for the FIB/SEM work. A 20 μm sided cube was sculpted from the middle of a compact Ca-rich particle, coated with Pt, and sliced with a 30 kV, 1.2nA Ga^+ beam. Images of each slice were acquired with a 5 kV electron beam and a back-scattered electron detector. The voxel size of the volume was 12x16x30 nm^3 and the size of the reconstructed volume was 20x10x6 μm^3. The images were aligned using DigitalMicrograph, and then median filtered and thresholded using Avizo.

2.6. Scanning transmission electron microscopy (STEM)

An electron-transparent specimen for scanning transmission electron microscopy (STEM) was created from the remainder of the tomography cube by lift-out and ion thinning with the FIB. A JEOL JEM-2100F microscope was used for imaging with an acceleration voltage of 200 kV. STEM was done with an annular dark-field detector providing mass (density) contrast. Elemental mapping was done with an Oxford X-MAX 80 EDS detector. Maps were generated in Oxford Aztec by integrating elemental Kα peaks and applying median filtering.

3. Results and discussion

3.1. Distribution of carbon nanofibers within cement matrix

Two different populations of nanofibers are present in the cement matrix. These are fibers present in the form of micro-sized aggregates as well as fibers evenly distributed within the cement matrix. Both types of structures were imaged using electron microscopy techniques.

The presence of aggregates was reveled using SEM-EDS imaging. The maps showing the distribution of oxygen and carbon in the cement are presented in Fig. 2. The areas free of oxygen (thus free of silicate) predominantly coincide with a high amount of carbon which suggests that some fraction of carbon nanofibers present in the cement form aggregates. The aggregates are tens to hundreds of micrometers in size. The REF sample is free of aggregates as it does not contain carbon nanofibers.

The carbon nanofibers distributed within the cement matrix were imaged using FIB-SEM tomography and FIB-STEM imaging. Due to the lower porosity and thus better imaging prospects of reacted cement, the imaging was performed for a particle extracted from the carbonated zone. Fig. 3a) shows the analyzed particle with embedded CNFs. Fig. 3b) shows the cubed particle ready for slicing and STEM sample extraction. The 3D dataset was thresholded to low intensity values as carbon fibers have lower intensity compared to the background carbonated cement matrix. Some pores and carbon particles of other shapes (e.g. spheres) are included in the thresholded volume shown in Fig. 3c. In total, the fibers and other carbon material, together with pores, occupy roughly 15 % of the analyzed volume. The white volume represents unconnected fibers or fibers belonging to smaller networks. The blue volume represents a large, connected network of fibers, where the brightness is always lower than the set threshold for distinguishing fiber from matrix.

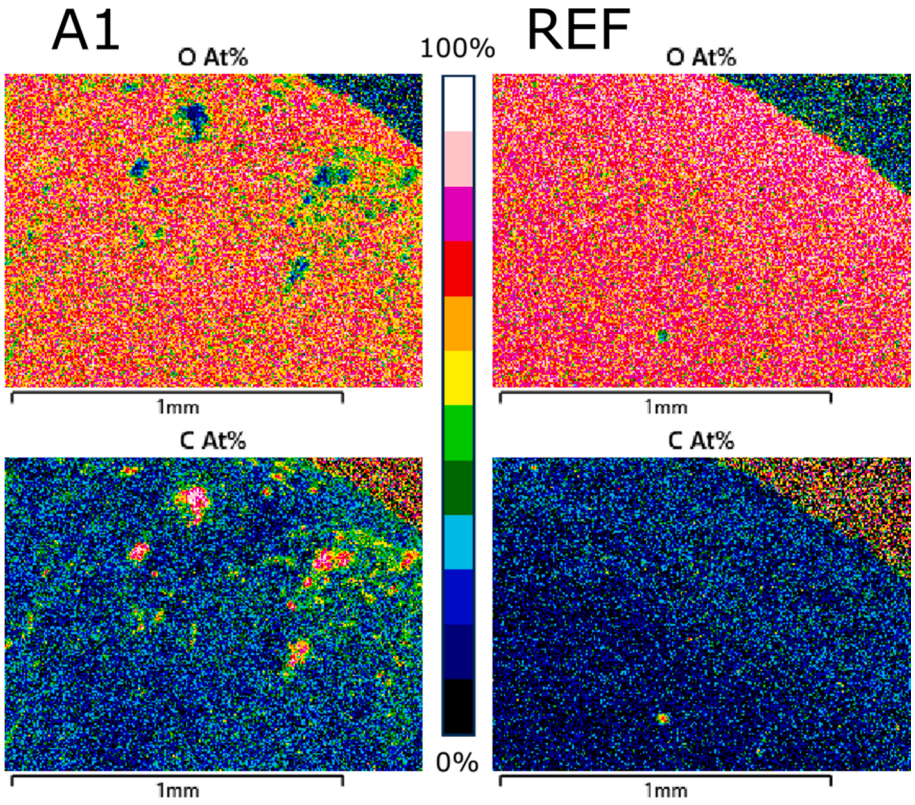

Fig. 2. Quantitative SEM-EDS maps showing distribution of carbon and oxygen in the A1 and REF samples.

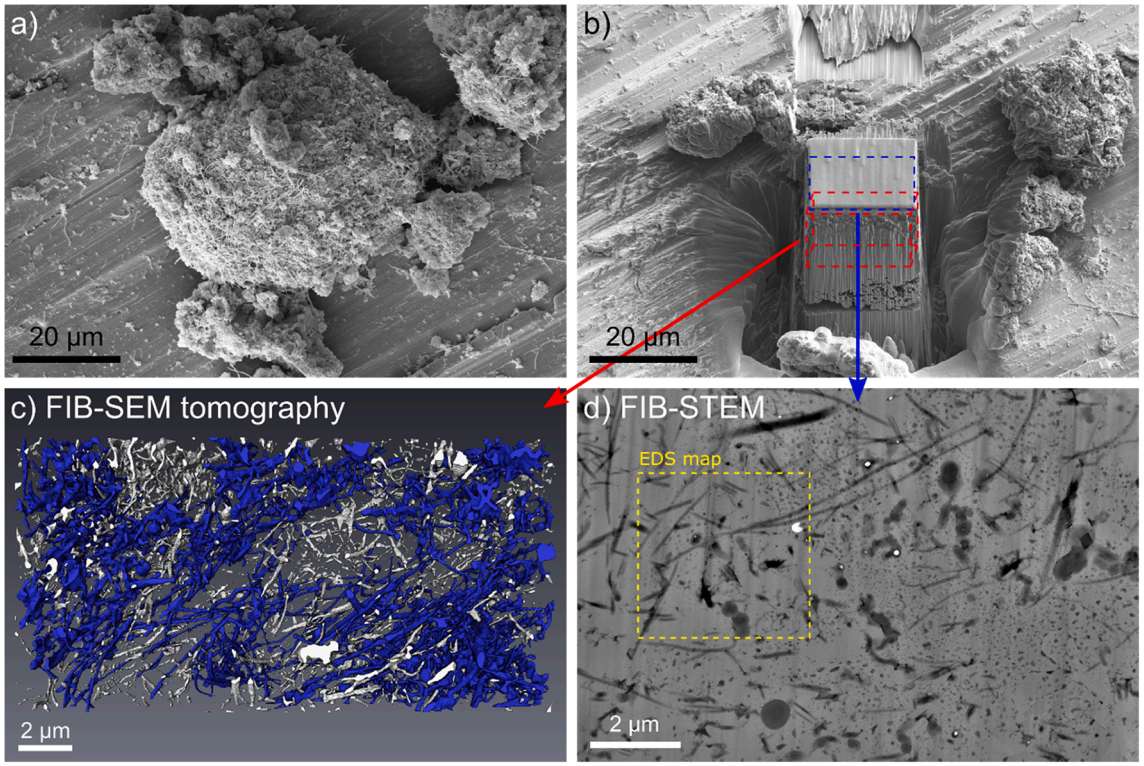

Fig. 3. Usage of FIB for tomography and TEM sample preparation from a cylinder shell particle. a) SEM image of the selected particle. b) SEM image of the particle after being shaped to a 20 µm sided cube. c) FIB-SEM volume thresholded to show carbon nanofibers. The blue fibers form a continuous network. d) Composite STEM image of a thinned lamella extracted from the cube in c). (For interpretation of the references to colour in this figure legend, the reader is referred to the web version of this article.)

The connected fiber volume spans a large region of the analyzed total volume and is in contact with all six side faces. In the analyzed particle the CNF therefore seems to form a percolating network.

To obtain electrical conductivity the percolation (connectivity) of the CNF network is crucial. The fibers do not have to be in direct contact to form electrically conductive paths, but the distances between them need to be shorter than the tunneling distance i.e. the distance below which electron transfer via tunneling mechanism can occur. The tunneling distance between carbon nanofibers is in the order of few nanometers in composite materials [28,29]. The resolution of FIB-SEM tomography presented here is in the order of 30 nm which poses limitations on predicting the actual electrical conductivity of the resulting material. Nevertheless, the tomography shows that the probability of having an electrically conductive network within a cement matrix is high despite of carbonation and a large number of CNFs aggregating.

The extracted and thinned specimen for STEM analysis is similar in size to the tomography slices. A composite STEM image of the specimen is shown in Fig. 3d). The image is high-pass filtered to even out variations in sample thickness. A richer selection of features is visible, including bright (heavy) particles and pores from 1 μm down to about 15 nm in size.

The elemental maps in Fig. 4 shed further light on the cement microstructure. Most of the carbon nanofibers are tubular, and the chemical maps as well as the STEM intensity indicate that they do not contain any solid material deposited inside. As carbon nanofibers are hydrophobic in nature [30] they may not allow ion-bearing aqueous solutions to penetrate inside their volume and deposit minerals. On the other hand, the calcium carbonate matrix seems to, rather tightly, adhere to the outside surfaces of the CNFs. The external surface of fibers might have been to some extent hydrophilized by the superplasticizer used to improve dispersibility of CNFs in cement [31]. In addition to carbon fibers, carbon spheres are also present in the cement. The carbon spheres, as well as iron and cerium bearing bright particles (only the Fe map is shown in Fig. 4), are most likely impurities from the CNF batch, since iron catalysts are often used in CNF synthesis [32]. Iron bearing particles may also originate from cement [33].

3.2. Dynamics of hybrid cement/CNF carbonation

Carbonation of the cement/CNF sample (A1) as well as the reference cement sample (REF) was followed in-situ using X-ray tomography imaging. Fig. 5 shows X-ray tomography cross sections through approximately the same areas of cement/CNF and the reference samples after 1, 7, 15, 24, 38, 59 days of exposure to CO_2-saturated water at atmospheric conditions. It is clear from the tomography images that while the reference sample is homogeneous, the cement/CNF sample has submillimeter dark spots corresponding to low density material. According to the SEM-EDS map in Fig. 2, this low density material is most likely CNF aggregates, although the presence of air bubbles cannot be excluded based on the tomography imaging only. The carbonation of cement samples is manifested in the darker rim proceeding from the outer surface towards the center of the samples. The carbonation of the reference cement sample proceeds in the form of stains growing from sample edges, while the carbonation of cement/CNF samples progresses as a uniform rim. To get a more quantitative understanding of the progress of carbonation over time, tomography images from Fig. 5 were integrated to form radial intensity profiles, as described in the *Materials and Methods* section. The profiles and their time evolution are presented in Fig. 6. The intensity variations are becoming less steep near the outer surface with increasing exposure time. The radius at which the profiles start departing (~5 % of intensity reduction) from the line representing the average intensity of the core region can be regarded as the location of the interface to non-carbonated material. From this, the thickness of the carbonated layer was found, the time evolution of which is shown in

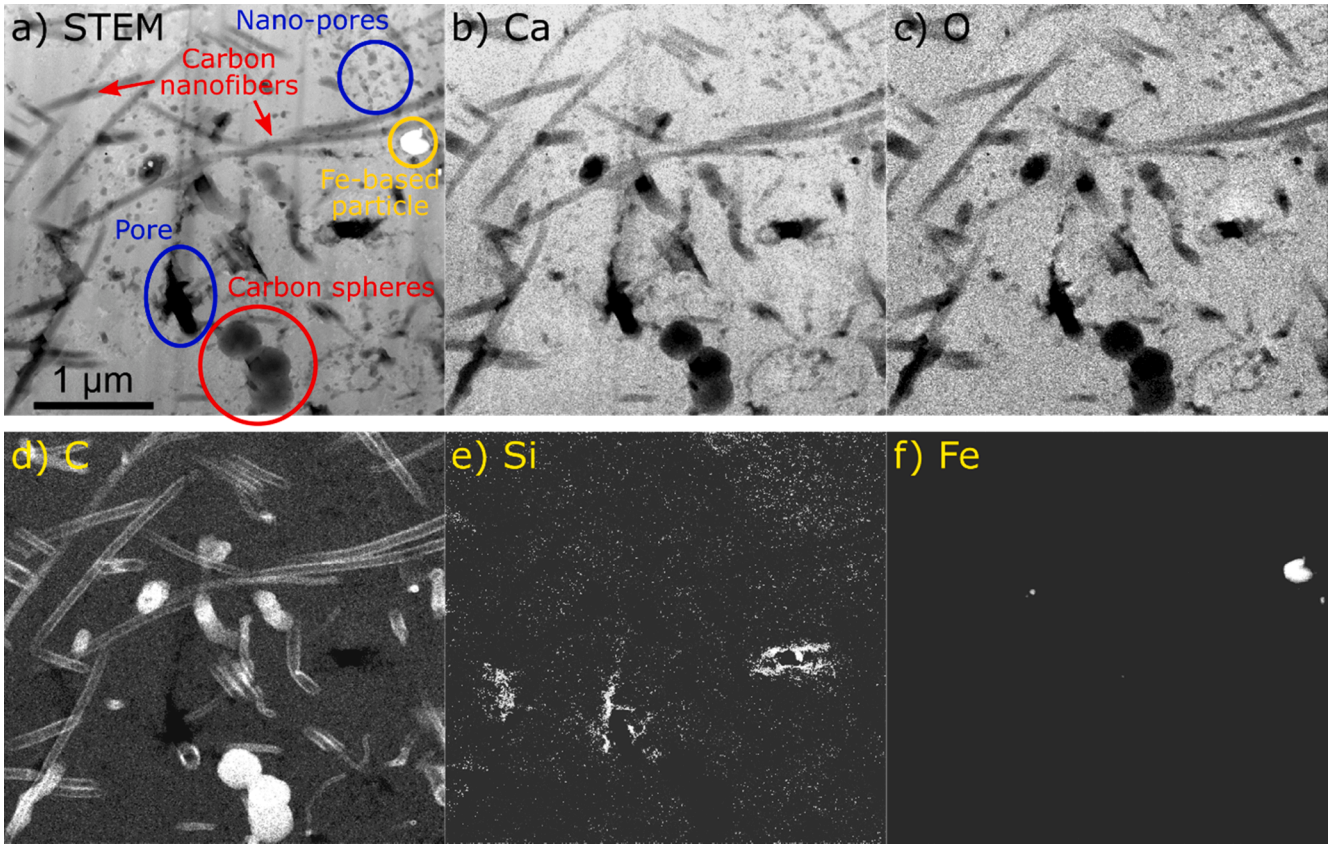

Fig. 4. STEM-EDS map of a region indicated in Fig. 2d); a) Annular dark-field STEM image with mass contrast; b–f) Elemental maps.

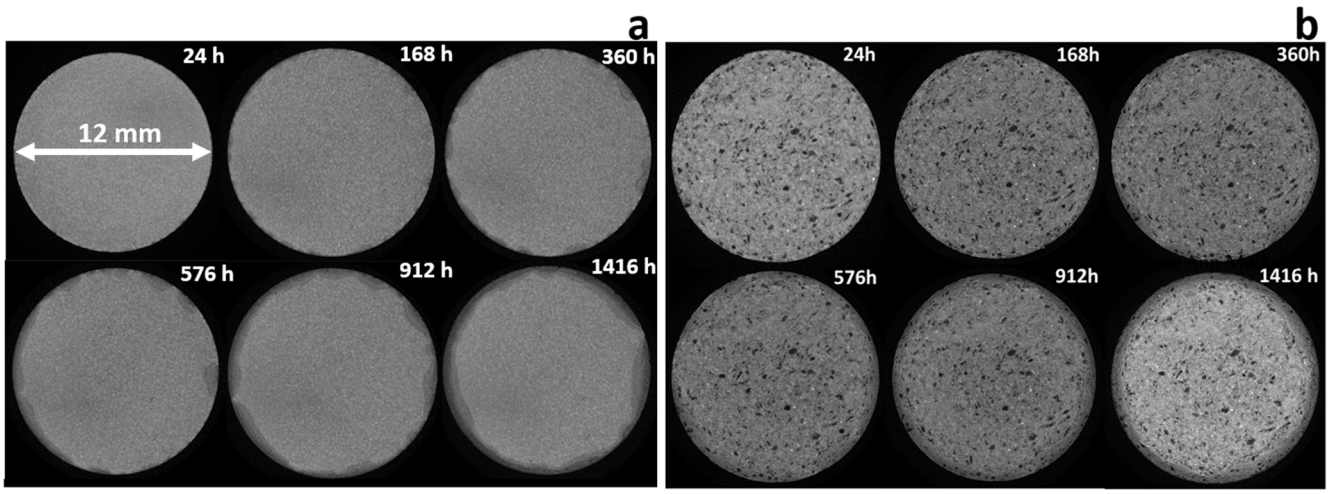

Fig. 5. CT cross-sections through the reference (a) and CNF/cement (A1) (b) samples after 1, 7, 15, 24, 38, 59 days of exposure to CO_2 saturated water at atmospheric conditions.

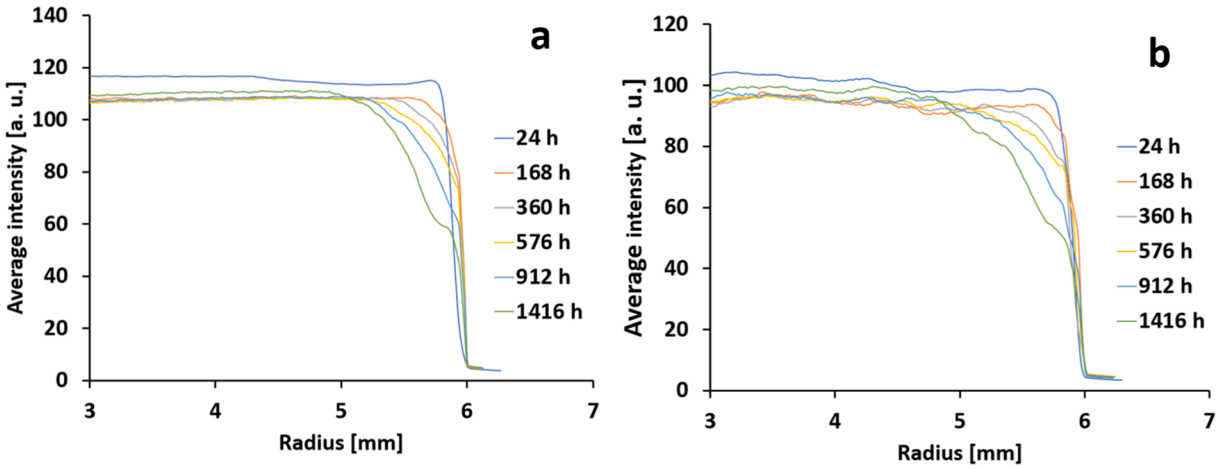

Fig. 6. Radial intensity profiles after 1, 7, 15, 24, 38, 59 days of exposure to CO_2 saturated water for the reference (a) and CNF/cement (A1) (b) samples. The sample center is at 0 mm radius while the sample edge is at 6 mm.

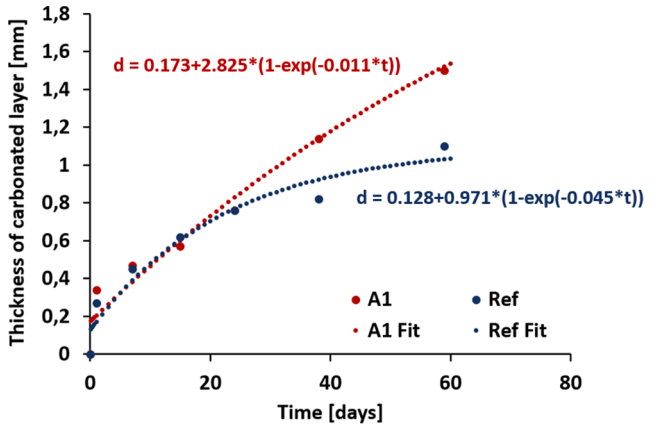

Fig. 7. Thickness of the carbonated layer (including porous silica depleted from calcium) as a function of time for the CNF/cement (A1) and the reference (Ref) samples.

Fig. 7. Within the studied timescale (up to 59 days) the growth of carbonated layer follows first order kinetics at the very beginning the carbonation process is very quick as the distance the carbonate ions need to diffuse into the cement are short; the distances get longer with the carbonation progress, thus the progress of the carbonation front slows down. The cement/CNF sample undergoes carbonation slightly faster compared to the reference cement sample. This is in line with observations made by Rodriguez et al. [34] who have reported more pronounced carbonation in Portland cement mortars with carbon nanotubes compared to mortars without carbon fillers. The authors have ascribed the faster carbonation to a more connected pore network present in mortars with carbon nanotubes and surfactants used to disperse them. According to authors, CNT may adsorb a portion of surfactant onto their surface, which is why, portion of surfactant will not be available to stabilizer air bubbles and may support generation of a more connected pore network. Similar effect could take place in our system. On the other hand Wang et al. reported reduction of carbonation depth for Portland cements with carbon nanofibers [35]. However, the content of CNFs in their work (0–0.5 wt%) was significantly lower than in our case (3 wt%). The authors also observed a reduction in the relative permeability coefficient upon addition of CNFs. The lowest value was obtained for 0.3 wt% CNF content. The relative permeability coefficient increased with increasing CNF content (from 0.3 to 0.5 wt%). Therefore, it is likely that further increase in CNF content may lead to accompanying increase in permeability. The CT images in Fig. 5 indicate more abundant inhomogeneities within the cement/CNF samples compared to

the REF sample. The presence of inhomogeneities, which is a result of very high CNF content, may contribute to higher and more connected porosity and thus increased permeability of the resulting hybrid material.

3.3. Resistivity changes during carbonation.

Conductivity of carbon nanofiber/cement composites typically has two contributions: (1) electronic associated with electron transfer within the fiber network and (2) electrolytic associated with the ion and mass transfer in the surrounding liquid [36]. The resistivity measured for the reference sample without carbon nanofibers before and after carbonation was over the reliable measurement limit (higher than tens of MΩ) which suggests that the electrolytic conductivity in the cement material was too small to be detected by the two-point measurements method used in this work. Thus, it has been suggested that the electronic conductivity via carbon nanofibers is the most dominant conduction mechanism contributing to conductivity (resistivity) measurements using the two-point method used in this paper.

Changes in resistance for the cement/CNF samples with different w/c ratios were followed for more than four months (136 days). The data are presented in Fig. 8. Since the dimensions of the samples were the same, the measured resistance is directly proportional to bulk resistivity with the same proportionality coefficient for all samples. Hence, the differences in resistance between the samples reflect a difference in bulk material properties only. Samples D1 and P1 have identical composition and dimensions, therefore the results obtained for the two samples show excellent reproducibility. The sample with lowest w/c ratio had the lowest resistance. This is in line with recently published studies by Gawel et al. [20]. The authors ascribed the low resistivity in samples with a low w/c ratio to a low amount of cement hydration products precipitated within the cement/CNF network. A higher w/c ratio yields a larger amount of precipitating hydration products. The precipitating crystals will disturb the pre-formed CNF conductive network [20]. Carbonation processes occurring inside wet cement material in contact with CO_2 also have a potential to affect resistivity of the cement/CNF material as they lead to structural changes within the cement. Indeed, the data in Fig. 8 suggest that cement/CNF material resistivity is affected by carbonation. During the first 50 days a quick resistivity increase is observed. Next, a plateau is reached, and the resistivity stabilizes and does not change significantly between 50 and 100 days of exposure. However, after 136 days of exposure a significant decrease in resistivity

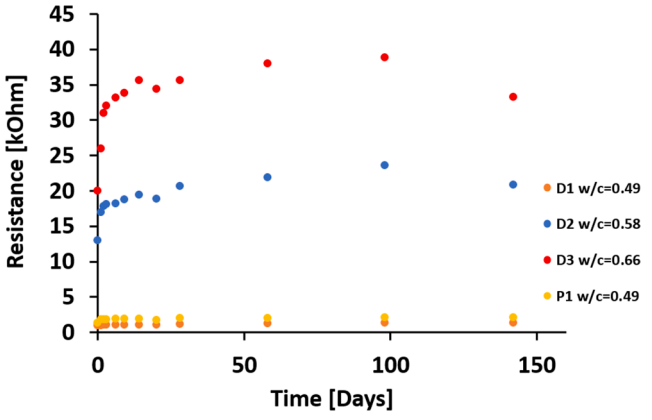

Fig. 8. Resistance vs. exposure time to CO_2-saturated water for cement/CNF samples with different w/c ratios. Resistance for the reference cement sample without carbon nanofibers was so high that it was beyond the measurements limit of the multimeter (higher than tens of MΩ) before and after carbonation. Resistance changes of D1 and P1 samples show good reproducibility. The trend observed for D1 and P1 is similar to D2 and D3 sample and only the magnitude of changes is smaller.

is observed. To better understand the underlying mechanism of the observed changes it is important to recall the main chemical and physical alterations occurring in cement upon carbonation.

When water saturated with CO_2 enters the cement matrix, the carbonic acid present in the solution starts reacting with cement hydration products i.e. calcium hydroxide (portlandite, $Ca(OH)_2$, CH in cement chemist notation) and calcium silicate hydrate (CSH). First calcium hydroxide dissolves in the solution. Owing to this dissolution, the pH inside the cement matrix is high, typically between 11 and 13 [25]. Next the calcium hydroxide and CSH react with carbonate ions, following the reactions described in Eq. (1) and (2) [25].

$$Ca^{2+} + 2OH^- + H^+ + HCO_3^- \leftrightarrow CaCO_3(s) + 2H_2O \quad (1)$$

$$2H^+ + CO_3^{2-} + C-S-H \leftrightarrow CaCO_3(s) + H_2O + amorphous-SiO_2 \quad (2)$$

Scarcely soluble and thus easily precipitating, calcium carbonate ($CaCO_3$, here abbreviated to CC) is a main product of these reactions. A CC precipitation process leads to an increase in cement density inside the carbonated layer. This is due to the higher density of CC (2.71 g/cm^3) with respect to CH (2.21 g/cm^3) [37]. The carbonation layer is manifested in computed tomography (CT) images as a bright layer adjecent to a nonmodified cement core. It can be seen in Fig. 9, showing CT crosssections for the D1, D2 and D3 samples after different exposure time up to 136 days. The carboantion front, i.e. the interface between the nonmodified cement and the carbonated layer, is depicted in Fig. 10a and schematically illustrated in Fig. 10b. It can be easily defined from the CT images. However, the interface between the carbonated layer and the calcium depleted layer that follows carbonation (the outermost layer) is difficult to distinguish based on CT contrast. The calcium depletion in this layer is due to dissolution of calcium carbonate from the carbonated layer. Due to carbonation the pH inside cement drops below 11 and the concentration of CO_3^{2-} decreases, and bicarbonate ions, HCO_3^-, begin to dominate. As a result, calcium carbonate is converted to water-soluble calcium bicarbonate according to reaction from Eq. (3):

$$CaCO_3(s) + H^+ + HCO_3^- \leftrightarrow Ca^{2+} + 2HCO_3^- \quad (3)$$

The reaction between CC and carbonic acid leads to leaching of calcium from the cement matrix. As a result a porous, amorphous silica rich layer is formed [25]. The layer has a significantly lower density and is seen as a dark rim propagating more or less regularly towards the centre of the cement/CNF samples (see Figs. 9 and 10).

The resistivity of the samples at the beginning of the carbonation process (first hours/days) is significantly increasing. At this stage of carbonation, the pH inside the cement matrix is high and the carbonated layer is formed at the sample outskirts. The leaching of $CaCO_3$ does not start before sufficiently low pH in the cement matrix is achieved [24,38] thus the porous layer from which CC is leached starts forming at a later stage than the carbonated layer. Thus at the very beginning of the carbonation the reacted volume is constituted mainly by the carbonated layer. The precipitating CC occupies a larger volume compared to the stoichiometric amount of the reacting CH [22]. This contributes to a reduced porosity of the cement matrix within the carbonated layer [22] and can affect the pre-established, during cement hydration process, CNF network. The resistivity increase at this stage suggests that the formation of calcium carbonate contributes to a decrease in connectivity between fibers. We suggest the following mechanism: The stoichiometric amount of CC crystals grows in the areas between fibers, leading to an increased separation between them. This is schematically illustrated in Fig. 11 a-b. The growing crystals may affect connections between single nanofibers distributed within the cement matrix but they can also break electrical connectivity within microsized fiber aggregates. The tomography images presented in Fig. 9 depict that the calcium depleted porous silica zone is established after seven days of

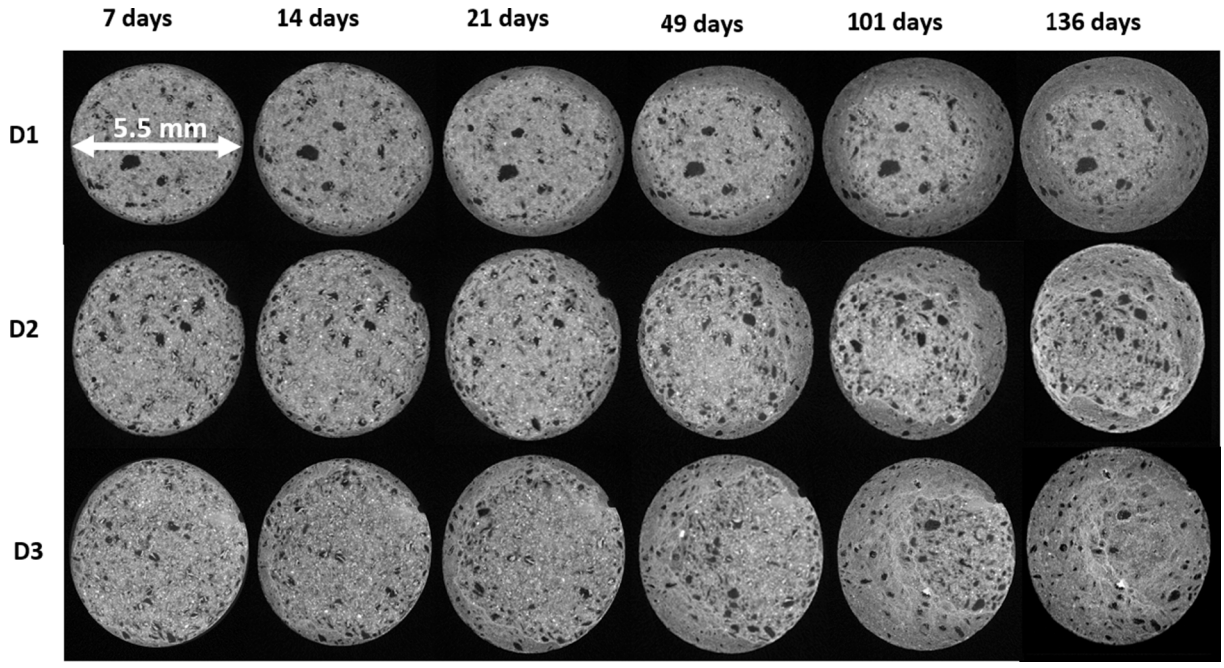

Fig. 9. CT crossections through D1, D2 and D3 samples after 7, 14, 21, 49, 101 and 136 days of exposure to CO_2-saturated water at atmospheric conditions.

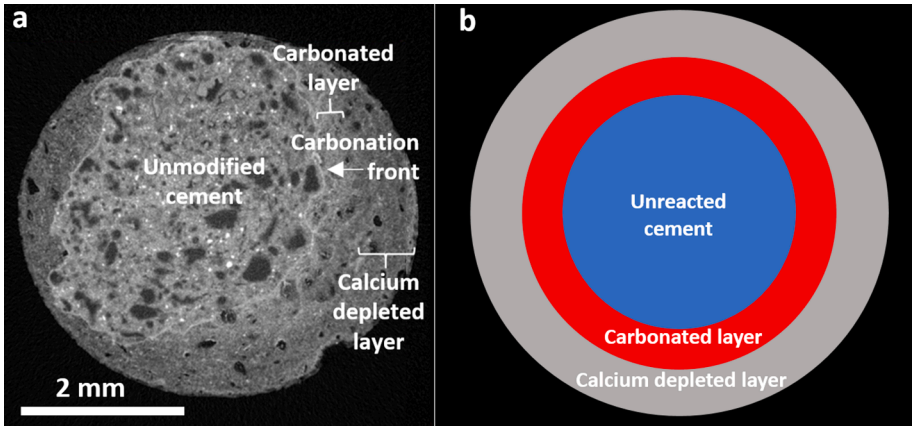

Fig. 10. a) X-ray tomography cross-section through sample D2 after 136 days of exposure to CO_2 saturated solution with indicated carbonated and calcium depleted layers; b) Schematic representation of different layers inside the cement sample exposed to CO_2: unreacted cement present in the most central region (blue), carbonated layer rich in CC (red) adjacent to the outermost calcium depleted, silica rich, porous layer (grey). (For interpretation of the references to colour in this figure legend, the reader is referred to the web version of this article.)

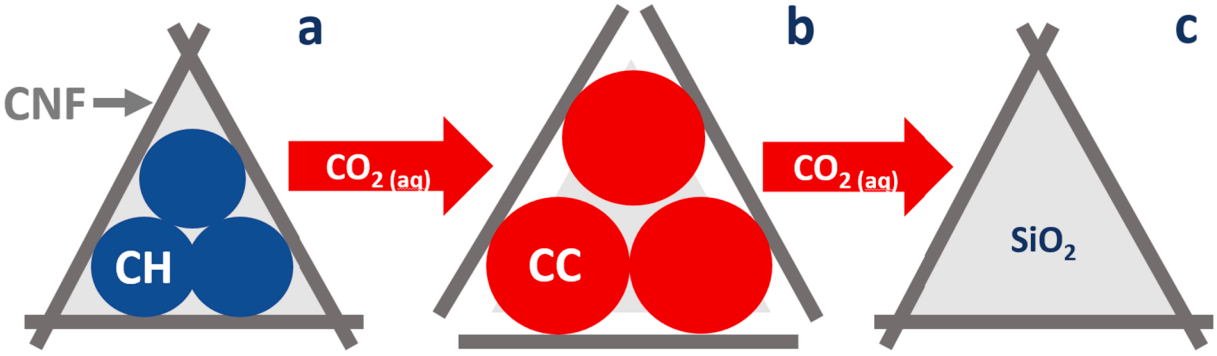

Fig. 11. Schematic illustration of mechanisms potentially responsible for the observed increase (first stage) and decrease (last stage) in resistivity upon carbonation: (a) The CNF network is established within the cement matrix made of unhydrated and hydrated cement particles and hydration products (CH); (b) The connectivity of the cement matrix decreases due to precipitation of CC that occupies a larger volume compared to substrate CH; (c) CC is removed from the cement fabric and CNFs are embedded in the remaining siliceous matrix (SiO_2). Due to leaching of CC the connectivity in the CNF network can to some extent be regained.

carbonation. Etching of calcium carbonate from the cement/CNF matrix has a potential to reconstitute the connectivity between fibers in this zone and hindering further rise of the net resistivity of the sample. This has been schematically illustrated in Fig. 11 b-c. Indeed, after 50 days of carbonation a plateau on the resistivity curve is reached (see Fig. 8). When the volume of calcium depleted layer starts to dominate over the carbonated layer the resistivity drops (conf. Fig. 8. and 9.). It is thus suggested that the two carbonation stages i.e. CC precipitation and leaching have contrary effect on the resistance within these layers. The total resistance in the carbonating cement/CNF sample is a net result of resistances within different reacted zones. It can be speculated that continuation of the carbonation process would result in a further decrease in sample resistivity.

The w/c ratio affects both degree of hydration and porosity of the cement paste. Higher w/c ratio leads to a higher porosity. The porosity differences may affect carbonation rate and thus indirectly impact associated resistivity changes. It is however difficult to separate the two effects (the effect of porosity and the effect of hydration degree) on resistivity. Theoretically, increased porosity should allow for increased ionic conductivity however what we observe is rather reduction of conductivity with increasing water content thus we hypothesize that differences in conductivity between samples are rather connected with the amount of hydration products precipitated than porosity differences between samples.

The suggested nanoscale mechanism is in line with the observations of microsized CNF aggregates from different zones (unreacted, carbonated and porous silica/CC depleted). Fig. 12 shows the difference between typical CNF aggregates present in the cement within the unreacted, carbonated and calcium depleted zone. The contrast differences between the aggregates from the three zones suggest that the CNFs located in the unreacted zone are assisted by the cement hydration products precipitated within the aggregate matrix. The product is most likely CH, similarly to cement pores in the hydrated Portland G cement reported elsewhere [22]. The high brightness within the aggregate from the carbonated zone suggests that the hydration products must have been transformed to CC product, which has a higher density and thus also higher attenuation of X-rays. In the outermost zone the calcium carbonate has leached out of the aggregate, leaving CNFs enclosed within the porous silica matrix. SEM imaging alone is not able to distinguish between empty pores and pores filled with CNFs. However, according to SEM-EDS imaging similar to that presented in Fig. 2, all the volumes free of oxygen (and thus silicate) that are visible at this scale are abundant in carbon, suggesting that all of them are filled with CNFs.

From the tomography data in Fig. 9, it is seen that after 136 days of carbonation, the reacted zone has advanced the furthest in sample D3. The largest unreacted volume is present in sample D1. The w/c ratio increases in the following order: D1 > D2 > D3. The higher carbonation rate observed for the sample with higher w/c ratio is in line with the observations made by others for cement pastes without carbon nanofibers [39]. A faster carbonation rate is typically ascribed to higher porosity and permeability in cement pastes with higher w/c ratios [39]. It has also been shown that cement pastes with higher w/c ratio give higher carbonation capacity i.e. a greater amount of CC can be precipitated during carbonation [39]. This is likely due to the larger amount of CH present in samples with higher w/c ratio. A semi quantitative analysis of CH content performed based on X-ray powder diffraction for identical compositions shows that the CH content increases with w/c ratio and is 8.1, 9.3 and 10.0 for samples D1 (w/c = 0.49), D2 (w/c = 0.58) and D3 (w/c = 0.66) samples respectively. Thus, the largest carbonation capacity is expected in sample D3, which may explain the largest increase in resistivity during carbonation observed in this sample.

4. Conclusions

This paper presents the results of studies on carbonation of conductive Portland G cement/carbon nanofiber composite materials. Carbonation of cement/CNF with different water/cement ratios was

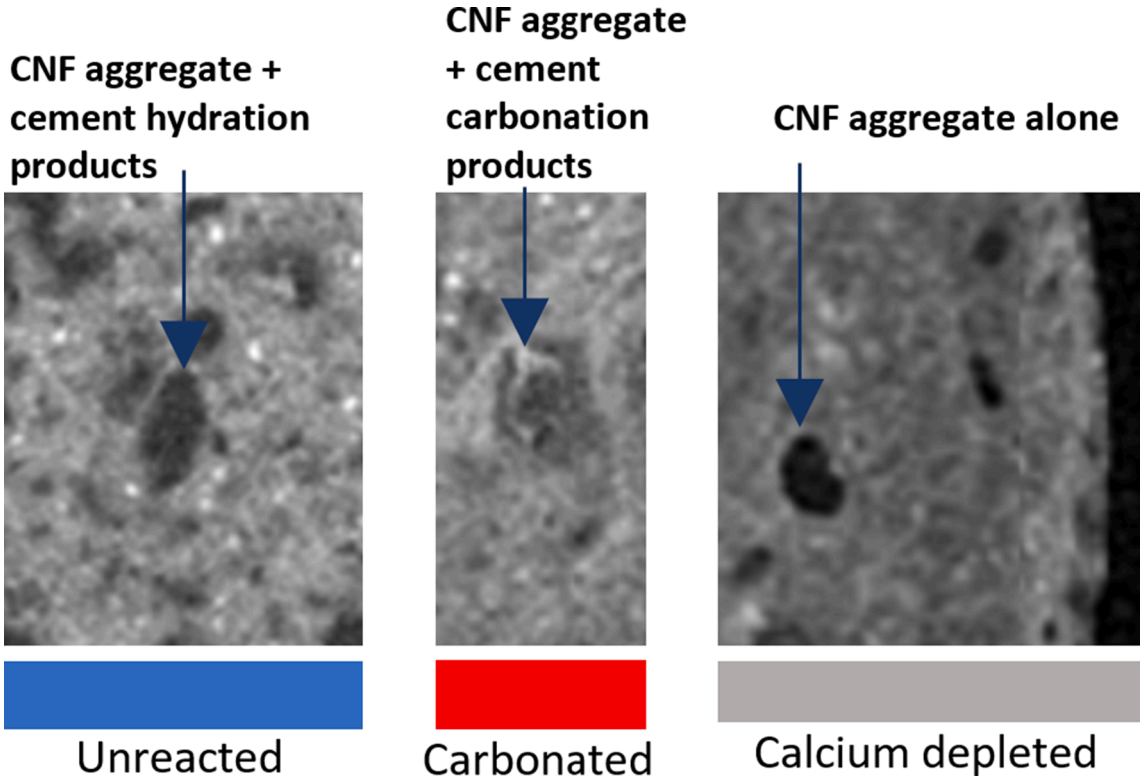

Fig. 12. X-ray tomography cross-sections through CNF aggregates from unreacted cement, carbonated cement and calcium depleted cement from sample D2 after 136 days of exposure to CO_2 saturated solution (cropped and magnified from Fig. 10 a).

performed at atmospheric conditions to mimic the deteriorative carbonation process occuring in construction elements in the environment. The composites were shown to host both aggregates of CNF and well-dispersed CNF forming a conductive network. The carbonation process was followed using X-ray tomography imaging and the progress of carbonation fronts were, for the first time, correlated with changes in resistivity.

It has been shown that cement materials with high content of carbon nanofibers (3 wt% in respect to cement powder) undergo faster carbonation compared to cement pastes without a conductive filler. An important new finding is that carbonation strongly affects the resistivity of cement/CNF materials. The two major stages of carbonation i.e. calcium carbonate precipitation and calcium carbonate dissolution have contrary effects on the sample resistivity. While calcium carbonate precipitation led to a resistivity increase, the dissolution resulted in a decrease. The magnitude of resistivity changes was strongly related with cement composite composition. More specifically, a higher water/cement ratio resulted in larger resistivity changes during carbonation. This was explained by a greater amount of calcium hydroxide undergoing volume-changing reactions.

Knowledge gained in this study needs to be taken into account at the stage of sensor material/transducer design as well as at the stage of data interpretation. Our findings open for other, new monitoring applications where chemical stability of cement-based construction elements can be monitored. The application areas for the chemical degradation sensors can be e.g. carbon dioxide storage, environmental monitoring, structural health monitoring, etc.

Cement carbonation is only one example of common degradation processes the cement materials may experience. It would therefore be of importance to define how other chemical degradation processes such as e.g. H_2S, H_2SO_4 acid attacks affect resistivity of cement/CNF materials and how the environmental degradation processes affect piezoresistive properties of cement/CNF composites.

CRediT authorship contribution statement

Kamila Gawel: Conceptualization, Data curation, Formal analysis, Funding acquisition, Investigation, Methodology, Project administration, Writing - original draft, Writing - review & editing. **Sigurd Wenner:** Data curation, Formal analysis, Investigation, Methodology, Writing - review & editing. **Laura Edvardsen:** Data curation, Formal analysis, Investigation, Methodology, Writing - review & editing.

Declaration of Competing Interest

The authors declare that they have no known competing financial interests or personal relationships that could have appeared to influence the work reported in this paper.

Acknowledgements

Financial support from SINTEF Industry strategic project SEP FARAWELL is gratefully acknowledged. The Research Council of Norway (RCN) is acknowledged for the support to the Norwegian Micro- and Nano-Fabrication Facility, NorFab, project number 245963/F50.The STEM work was performed under the auspices and infrastructure of the Norwegian Transmission Electron Microscopy Centre (NORTEM) supported by RCN, project number 197405. The use of the X-ray laboratory at NTNU is gratefully acknowledged.

References:

[1] D. Chung Electrically Conductive Cement-Based Mater. 16 2004 167 176.
[2] A. Meoni, A. D'Alessandro, A. Downey, E. García-Macías, M. Rallini, A. Materazzi, L. Torre, S. Laflamme, R. Castro-Triguero, F. Ubertini, An experimental study on static and dynamic strain sensitivity of embeddable smart concrete sensors doped with carbon nanotubes for shm of large structures, Sensors (Basel, Switzerland) 18 (3) (2018) 831, https://doi.org/10.3390/s18030831.
[3] F. Carmona, R. Canet, P. Delhaes, Piezoresistivity of heterogeneous solids, J. Appl. Phys. 61 (7) (1987) 2550–2557.
[4] X. Wang, X. Fu, D.D.L. Chung, Strain sensing using carbon fiber, J. Mater. Res. 14 (3) (1999) 790–802.
[5] M. Sun, et al., Study of piezoelectric properties of carbon fiber reinforced concrete and plain cement paste during dynamic loading, Cem. Concr. Res. 30 (10) (2000) 1593–1595.
[6] R.E. Newnham, L.J. Bowen, K.A. Klicker, L.E. Cross, Composite piezoelectric transducers, Mater. Des. 2 (2) (1980) 93–106.
[7] Z. Li, D. Zhang, K. Wu, Cement-based 0–3 piezoelectric composites, J. Am. Ceram. Soc. 85 (2) (2002) 305–313.
[8] B. Han, J. Ou, Embedded piezoresistive cement-based stress/strain sensor, Sens. Actuators, A 138 (2) (2007) 294–298.
[9] K. Ramam, K. Chandramouli, Piezoelectric cement composite for structural health monitoring, Adv. Cem. Res. 24 (3) (2012) 165–171.
[10] A.O. Monteiro, A. Loredo, P.M.F.J. Costa, M. Oeser, P.B. Cachim, A pressure-sensitive carbon black cement composite for traffic monitoring, Constr. Build. Mater. 154 (2017) 1079–1086.
[11] J. Zhang, Y. Lu, Z. Lu, C. Liu, G. Sun, Z. Li, A new smart traffic monitoring method using embedded cement-based piezoelectric sensors, Smart Mater. Struct. 24 (2) (2015) 025023, https://doi.org/10.1088/0964-1726/24/2/025023.
[12] S. Wen, D.D.L. Chung, Piezoelectric cement-based materials with large coupling and voltage coefficients, Cem. Concr. Res. 32 (3) (2002) 335–339.
[13] M. Saafi, Wireless and embedded carbon nanotube networks for damage detection in concrete structures, Nanotechnology 20 (39) (2009) 395502, https://doi.org/10.1088/0957-4484/20/39/395502.
[14] A. Downey, A. D'Alessandro, M. Baquera, E. García-Macías, D. Rolfes, F. Ubertini, S. Laflamme, R. Castro-Triguero, Damage detection, localization and quantification in conductive smart concrete structures using a resistor mesh model, Eng. Struct. 148 (2017) 924–935.
[15] S. Wen, D.D.L. Chung, Model of piezoresistivity in carbon fiber cement, Cement and Concrete Research 36 (10) (2006) 1879–1885.
[16] Dietrich Stauffer, A.A., Introduction to Percolation Theory. 1994.
[17] J.B. Czyzewski, P. Gawel, K. Meisner, J, Rapid prototyping of electrically conductive components using 3D printing technology, J. Mater. Process. Technol. 209 (12–13) (2009) 5281–5285.
[18] N. Yang, K. Zhang, Q. Sun, Dispersion and pressure sensitivity of carbon nanofiber-reinforced polyurethane cement, Appl. Sci. 8 (2018) 2375.
[19] L. Zhang, S. Ding, B. Han, X. Yu, Y.-Q. Ni, Effect of water content on the piezoresistive property of smart cement-based materials with carbon nanotube/nanocarbon black composite filler, Compos. A Appl. Sci. Manuf. 119 (2019) 8–20.
[20] K. Gawel, M.A. Taghipour Khadrbeik, R. Bjørge, S. Wenner, B. Gawel, A. Ghaderi, P. Cerasi, Effects of water content and temperature on bulk resistivity of hybrid cement/carbon nanofiber composites, Materials 13 (13) (2020) 2884, https://doi.org/10.3390/ma13132884.
[21] R. Bjørge, K. Gawel, E.A. Chavez Panduro, M. Torsæter, Carbonation of silica cement at high-temperature well conditions, Int. J. Greenhouse Gas Control 82 (2019) 261–268.
[22] E.A. Chavez Panduro, M. Torsæter, K. Gawel, R. Bjørge, A. Gibaud, A. Bonnin, C. M. Schlepütz, D.W. Breiby, Computed X-ray tomography study of carbonate precipitation in large portland cement pores, Cryst. Growth Des. 19 (10) (2019) 5850–5857.
[23] E.A. Chavez Panduro, et al., In-situ x-ray tomography study of cement exposed to CO<inf>2</inf> saturated brine, Environ. Sci. Technol. 51 (16) (2017) 9344–9351.
[24] E.A. Chavez Panduro, et al., Real time 3d observations of portland cement carbonation at CO<inf>2</inf>storage conditions, Environ. Sci. Technol. 54 (13) (2020) 8323–8332.
[25] B.G. Kutchko, B.R. Strazisar, D.A. Dzombak, G.V. Lowry, N. Thaulow, Degradation of well cement by co2 under geologic sequestration conditions, Environ. Sci. Technol. 41 (13) (2007) 4787–4792.
[26] V.T. Ngala, C.L. Page, Effects of carbonation on pore structure and diffusional properties of hydrated cement pastes, Cem. Concr. Res. 27 (7) (1997) 995–1007.
[27] V.G. Papadakis, C.G. Vayenas, M.N. Fardis, Fundamental modeling and experimental investigation of concrete carbonation, ACI Mater. J. 88 (4) (1991) 363–373.
[28] Y. Zare, K.Y. Rhee, Simulation of percolation threshold, tunneling distance, and conductivity for carbon nanotube (cnt)-reinforced nanocomposites assuming effective cnt concentration, Polymers 12 (1) (2020) 114.
[29] Z. Liu, W. Peng, Y. Zare, D. Hui, K.Y. Rhee, Predicting the electrical conductivity in polymer carbon nanotube nanocomposites based on the volume fractions and resistances of the nanoparticle, interphase, and tunneling regions in conductive networks, RSC Adv. 8 (34) (2018) 19001–19010.
[30] N. Baig, F.I. Alghunaimi, T.A. Saleh, Hydrophobic and oleophilic carbon nanofiber impregnated styrofoam for oil and water separation: a green technology, Chem. Eng. J. 360 (2019) 1613–1622.
[31] M. Liebscher, A. Lange, C. Schröfl, R. Fuge, V. Mechtcherine, J. Plank, A. Leonhardt, Impact of the molecular architecture of polycarboxylate superplasticizers on the dispersion of multi-walled carbon nanotubes in aqueous phase, J. Mater. Sci. 52 (4) (2017) 2296–2307.
[32] A.V. Melechko, V.I. Merkulov, T.E. McKnight, M.A. Guillorn, K.L. Klein, D. H. Lowndes, M.L. Simpson, Vertically aligned carbon nanofibers and related structures: controlled synthesis and directed assembly, J. Appl. Phys. 97 (4) (2005) 041301, https://doi.org/10.1063/1.1857591.

[33] A. Monshi, M.K. Asgarani, Producing portland cement from iron and steel slags and limestone, Cem. Concr. Res. 29 (9) (1999) 1373–1377.
[34] B. Rodriguez, et al., Carbonation study in a cement matrix with carbon nanotubes, J. Phys. Conf. Ser. 1247 (2019), 012024.
[35] T. Wang, et al., Experimental study on the effect of carbon nanofiber content on the durability of concrete, Constr. Build. Mater. 250 (2020), 118891.
[36] S. Wen, D.D.L. Chung, The role of electronic and ionic conduction in the electrical conductivity of carbon fiber reinforced cement, Carbon 44 (11) (2006) 2130–2138.
[37] H.E. Mason, S.D.C. Walsh, W.L. DuFrane, S.A. Carroll, Determination of diffusion profiles in altered wellbore cement using x-ray computed tomography methods, Environ. Sci. Technol. 48 (12) (2014) 7094–7100.
[38] B. Šavija, M. Luković, Carbonation of cement paste: understanding, challenges, and opportunities, Constr. Build. Mater. 117 (2016) 285–301.
[39] S. Siddique, A. Naqi, J.G. Jang, Influence of water to cement ratio on CO2 uptake capacity of belite-rich cement upon exposure to carbonation curing, Cem. Concr. Compos. 111 (2020), 103616.